Physics in Medicine &
Biology

Monte Carlo-based scatter correction for the plastic-based modular PET scanner J-PET

To cite this article before publication: Reimund Bayerlein *et al* 2026 *Phys. Med. Biol.* in press https://doi.org/10.1088/1361-6560/ae54fb

Monte Carlo-Based Scatter Correction for the Plastic-Based Modular PET Scanner J-PET

Reimund Bayerlein[1,2*], Manish Das[3,4,5*], Sushil Sharma[3,4,5], Ramsey D. Badawi[2,1], Ermias Yitayew Beyene[3,4,5], Neha Chug[3,4,5], Catalina Curceanu[6], Eryk Czerwiński[3,4,5], Kavya Valsan Eliyan[3,4,5], Jakub Hajduga[7], Alicja Hubalewska-Dydejczyk[8], Sharareh Jalali[3,4,5], Krzysztof Kacprzak[3,4,5], Tevfik Kaplanoglu[3,4,5], Łukasz Kapłon[3,4,5], Kamila Kasperska[3,4,5], Aleksander Khreptak[3,4,5], Grzegorz Korcyl[3,4,5], Tomasz Kozik[3,4,5], Karol Kubat[3,4,5], Sumit Kumar Kundu[3,4,5], Anoop Kunimmal Venadan[3,4,5], Deepak Kumar[3,4,5], Edward Lisowski[8], Filip Lisowski[8], Justyna Mędrala-Sowa[3,4,5], Simbarashe Moyo[3,4,5], Wiktor Mryka[3,4,5], Szymon Niedźwiecki[3,4,5], Marta Opalińska[8], Piyush Pandey[3,4,5], Anand Pandey[3,4,5], Szymon Parzych[3,4,5], Alessio Porcelli[3,4,5,6,10], Bartłomiej Rachwał[7], Martin Rädler[3,4,5], Benjamin A. Spencer[2,1], Anna Sowa-Staszczak[8], Magdalena Skurzok[3,4,5], Tomasz Szumlak[7], Satyam Tiwari[3,4,5], Pooja Tanty[3,4,5], Keyvan Tayefi Ardebili[3,4,5], Ewa Ł. Stępień[3,4,5] and Pawel Moskal[3,4,5]

[1] Department of Biomedical Engineering, University of California Davis, Davis, USA
[2] Department of Radiology, University of California Davis, Sacramento, USA
[3] Faculty of Physics, Astronomy and Applied Computer Science, Jagiellonian University, Krakow, Poland
[4] Total-Body Jagiellonian-PET Laboratory, Jagiellonian University, Krakow, Poland
[5] Center for Theranostics, Jagiellonian University, Krakow, Poland
[6] INFN, Laboratori Nazionali di Frascati CP 13, Frascati, Italy
[7] AGH University of Krakow, Poland.
[8] Cracow University of Technology, Faculty of Mechanical Engineering, Kraków, Poland
[9] Chair and Department of Endocrinology, Jagiellonian University Medical College, Kraków, Poland
[10] Center of Astronomical Research, Technology, Education, and Outreach, University of Antofagasta, Antofagasta, Chile

*The authors contributed equally
E-mail: rbayerlein@ucdavis.edu, manish.das@doctoral.uj.edu.pl

December 2025

Abstract. *Objective.* This work presents and evaluates a Monte Carlo–based scatter correction (SC) method developed for the Jagiellonian Positron Emission Tomography (J-PET) scanner, a modular PET system based on plastic scintillators.

Approach. The algorithm employs SimSET-based simulations integrated into a time-of-flight ordered-subsets expectation maximization (TOF-OSEM) reconstruction framework to estimate scatter contributions. Phantom studies using the NEMA IQ phantom and a proof-of-principle human subject scan with the J-PET scanner were analyzed. To accelerate computation, LYSO crystals were also assessed in simulations as a surrogate for the native plastic material BC-404.

Main results. In phantom experiments, SC improved contrast recovery coefficients (CRC) by over 20% and reduced background variability (BGVar) by 8.5%, without introducing significant noise. Residual activity in cold regions was also considerably reduced. Substituting LYSO in the simulations decreased runtime by nearly one order of magnitude, while maintaining deviations below 6% in image quality metrics compared to BC-404. Human subject data demonstrated qualitatively reduced residual scatter and improved organ delineation. Quantitative comparison with the commercial PET/CT scanner GE Discovery MI Gen 2 showed consistent activity

concentration ratios across organs, although higher noise and residual scatter between organs were observed in J-PET, which most likely originates from lower count density.

Significance. The proposed MC-based SC method provides robust scatter removal for J-PET, improving quantitative performance and establishing a foundation for advanced correction and reconstruction techniques. These results bring the plastic scintillator-based J-PET scanner closer to enabling clinically relevant quantitative PET imaging.

Key Words: Scatter Correction (SC), Monte Carlo (MC) Simulation, Plastic scintillators, J-PET scanner, Image quality assessment

Introduction

Positron Emission Tomography (PET) is a powerful molecular imaging technique that enables the three-dimensional visualization of metabolic processes in the human body and has become an essential tool in nuclear medicine diagnostics (Gurunath Bharathi *et al.*, 2025). However, conventional PET systems rely on a large number of electronic read-out channels as well as expensive inorganic scintillators, which limit their accessibility and cost-effectiveness. The modular and lightweight J-PET (Jagiellonian Positron Emission Tomography) scanner offers an innovative alternative by utilizing 50-cm-long polymer scintillator strips coupled to photon detectors on both ends (Moskal *et al.*, 2024). Although plastic scintillators have lower attenuation for PET-typical photon energies and lower energy resolution, they have the potential to exhibit exceptional temporal resolution (Moskal *et al.*, 2016),(Sharma *et al.*, 2023), and enable construction of portable and cost-effective PET systems (Vandenberghe, Moskal and Karp, 2020).

One of the key challenges in PET imaging is the accurate correction of scattered events, which occur if one or both emitted 511-keV photons scatter once or multiple times in the subject within or outside the field-of-view (FOV). This can introduce image artifacts, quantitative biases, and reduce diagnostic reliability (Zaidi and Montandon, 2007). Simulations of the J-PET scanner in prior works have shown a scatter fraction (SF) ranging from 36.3% to 41.7±0.2% (Moskal *et al.*, 2021; Ardebili, Niedźwiecki and Moskal, 2023; Ardebili and Moskal, 2024), underscoring the necessity for effective scatter correction (SC) methods to enable quantitative imaging. The aim of this study was to develop a SC algorithm tailored to the J-PET system and to evaluate it using phantom and human subject studies. To this end, we have chosen a Monte Carlo (MC)-based approach for two main reasons. While single scatter simulation (SSS) has been one of the most commonly used correction technique for scatter (Watson, 2000), MC methods have proven to be reliable and accurate and were historically seen as gold standard, since they enabled the separation of scattered and unscattered (true) events (Zaidi, 2000). Secondly, the method follows an established algorithm developed for the uEXPLORER total-body PET/CT scanner, which has previously proven its accuracy in modeling complex scatter interactions (Bayerlein *et al.*, 2024).

In this work we will provide a rigorous phantom evaluation of the proposed SC method using the NEMA image quality (IQ) phantom (National Electrical Manufacturers Association, 2018), which allows us to quantitatively assess key image quality metrics. We will then present and – for the first time – evaluate the scatter correction in a PET scan of a human subject scanned on the J-PET scanner.

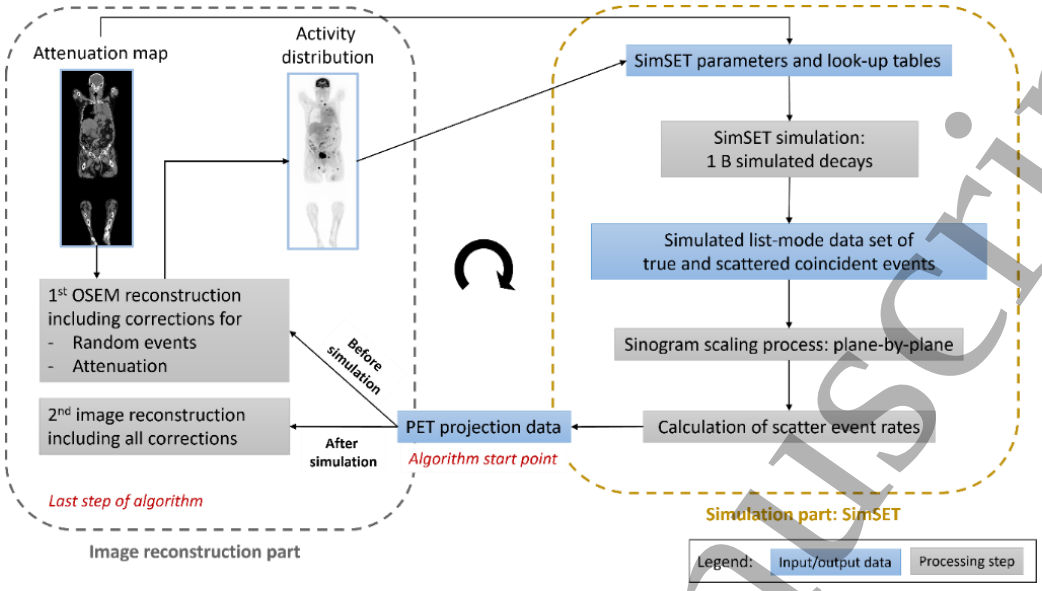

Figure 1: Flow chart of the scatter correction and image reconstruction framework for the modular J-PET scanner. This SC correction algorithm is performed once using the first uncorrected image reconstruction, before the calculated scatter event rates are used in a second OSEM image reconstruction providing a fully corrected PET image.

Materials and Methods

Overview of the scatter correction method

We implemented a Monte Carlo-based approach to quantify the contribution of scattered events to each line of response (LOR) and time-of-flight bin. This approach was integrated into an iterative list-mode time-of-flight (TOF) ordered-subsets expectation maximization (OSEM) reconstruction scheme. An overview of the processing pipeline is shown in Figure 1. Scatter estimation was performed in between two reconstruction iterations. In the first reconstruction step, an initial activity image was generated with corrections applied for random coincidences and attenuation, while scatter correction was intentionally omitted. Dead-time correction was not applied, as event rates in the J-PET system are sufficiently low. At this stage, the reconstruction relied solely on the raw list-mode data and normalization factors; all applied corrections followed the methodology described in our previous work (Das, Bayerlein, and et al., 2024). The resulting preliminary image served as the activity input for Monte Carlo simulations using SimSET (version 2.9.2). A corresponding attenuation map was derived from CT data via bilinear transformation according to (Carney *et al.*, 2006) and subsequently converted into the attenuation index format required by SimSET. The simulation workflow – including generation of list-mode data, rebinning into true and scatter sinograms, and sinogram scaling – was carried out following the procedure detailed in (Bayerlein *et al.*, 2024). Based on these results, event-wise scatter estimates were computed and incorporated into the subsequent OSEM update step.

J-PET scanner geometry and statistical considerations

The modular J-PET scanner is shown in Figure 2 together with the NEMA IQ phantom on the patient bed. The J-PET scanner enables data taking with TOF resolution of 220 ps, an energy

resolution of 16% and provides a NEMA sensitivity of 1.03 ± 0.02 kcps/MBq with a peak sensitivity of 2.1 kcps/MBq (Ardebili, Niedźwiecki and Moskal, 2023). The spatial resolution for TOF image reconstruction is 4.92 ± 0.56 mm, 7.38 ± 0.51 mm and 30.73 ± 0.52 mm FWHM in radial, tangential and axial direction, respectively (Ardebili and Moskal, 2024). Data taking is performed with a data acquisition server. The data is then stored on Linear Tape-Open (LTO) generation 9 cartridges, which are housed in the tower indicated as "tape library" in Figure 2.

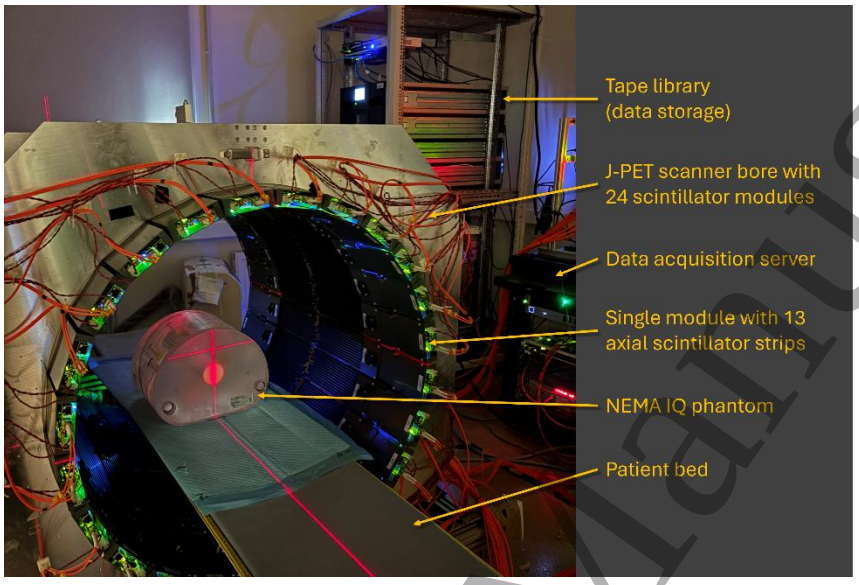

Figure 2: J-PET scanner with equipment and the NEMA IQ phantom on the patient bed.

The J-PET scanner is composed of 24 transaxial modules, each housing 13 plastic scintillator strips with an axial length of 50 cm, resulting in a total of 312 transaxial scintillators. Each strip has a cross section of 6 mm in the transaxial direction and 24 mm in depth (Moskal *et al.*, 2021). To form a valid coincidence, two scintillator strips must be separated by at least 60 degrees in the transaxial plane, meaning there are 208 strips that can form a coincidence per projection angle. For sinogram generation, the axially continuous scintillator strips were segmented into 200 2.5-mm long axial pseudo-crystals. With interleaving, this configuration produces 207 lines of response per projection angle, across 156 angular views and 200 × 200 possible detector planes. In total, the scanner geometry comprises 1,291,680,000 distinct LORs, making direct scatter estimation at the individual LOR level computationally very challenging. Thus, groups of four transaxial scintillator strips and eight axial pseudo-crystals were combined into block pairs with dimensions of 20 mm × 24 mm. Each block pair represents $(4 \cdot 8)^2 = 1024$ combined LORs, substantially lowering the computational burden while preserving the essential geometric structure.

This allows for a variance reduction on the estimate of scatter per sinogram bin. A similar block size has been successfully implemented by (Bayerlein *et al.*, 2024). Since scatter is a low frequency phenomenon in projection space, we can on average assume equal distribution of scattered events over all LORs per block pair. With 51 block-based projection bins, 39 angles and 25 axial blocks, the total number of block pairs in the scanner is 1,243,125. Thus, the number of simulated true and scattered events collected in a block pair is three orders of magnitude higher than in a pseudo-crystal-based LOR.

Image reconstruction framework

Image reconstruction was performed using a time-of-flight (TOF) ordered subsets expectation maximization (OSEM) framework implemented using Customizable and Advanced Software for Tomographic Reconstruction (CASToR) (Merlin *et al.*, 2018). In this study, the sensitivity map was derived entirely from Monte Carlo (MC) simulations and applied during reconstruction, as described in (Das, Bayerlein, and et al., 2024). Additionally, normalization was also applied during reconstruction using a component-based method (Badawi and Marsden, 1999; Pépin *et al.*, 2011). Additionally, a point spread function (PSF) model was incorporated during reconstruction to enhance spatial resolution. For the phantom studies, 10 iterations and 4 subsets were used. For the human subject study, 10 iterations were performed without subset acceleration. Due to the low count rate in the human dataset, the number of iterations was limited to prevent excessive amplification of image noise. A Gaussian post-reconstruction smoothing filter with a 5-mm kernel was applied in all cases.

Implementation of scintillator materials in SimSET

The J-PET detector utilizes BC-404 plastic scintillators, manufactured by Eljen Technology. The BC-404 scintillator is based on polyvinyltoluene (PVT), with the chemical composition $C_{10}H_{11}$ and a density of 1.023 g/cm³ (Kapłon *et al.*, 2025). These properties were used to define the material in the SimSET simulation environment. However, due to the inherently lower attenuation of plastic for 511-keV photons compared to commonly used scintillator crystals, the detection sensitivity and, thus, the simulation run times are very long. Therefore Lutetium–yttrium oxyorthosilicate (LYSO) was also implemented as a more efficient and faster alternative. In the scope of this work, we performed a quantitative comparison of the impact of material choice on image quality metrics like contrast and background noise to investigate if LYSO can be safely used as surrogate material in our MC-simulations and SC.

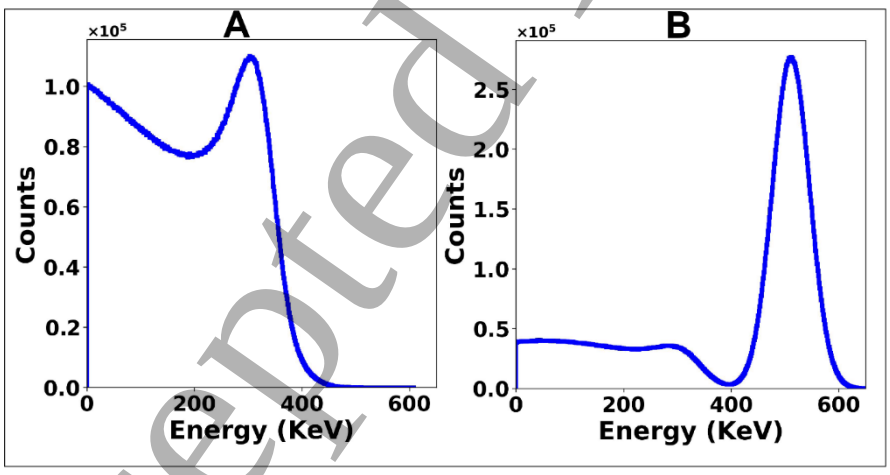

Figure 3. The spectra of the deposited energy for the true events simulated with SimSET with (A) BC-404 (B) LYSO.

In a first step to assess the correctness of the simulation, the energy spectra for true events obtained with the BC-404 scintillator and LYSO, both simulated using 511 keV decays and a 16% detector energy resolution, are shown in Figure 3. The energy spectrum for BC-404 is presented in Figure 3 (A), while that for LYSO is shown in Figure 3 (B). The BC-404 spectrum shows that interactions in the plastic scintillator are primarily due to Compton scattering, with

the Compton edge located at around 341 keV. In our comparative analysis, we also recorded the required computation times and the obtained scatter thresholds for the NEMA IQ times using LYSO and BC-404, respectively. The results can be found in table 1.

Monte Carlo-Based Estimation of Scatter using SimSET

This MC-based SC method was originally developed for the uEXPLORER total-body PET/CT scanner, which uses LYSO as scintillator material instead of plastic (Bayerlein *et al.*, 2024). Due to plastic's low attenuation for 511-keV photons, the detection efficiency is considerably lower. Therefore, also the run-time of the simulation exceeds practical limits if a high-count data set is to be acquired. For phantom simulations we used both materials in our simulations and scatter correction to investigate whether the computational benefits of using LYSO can be exploited without loss of accuracy. Five billion radioactive decays of F-18 were simulated using LYSO, and 200 billion radioactive decays were simulated using plastic. These numbers resulted in approximately the same number of collected coincidences in the simulation making the data sets comparable in size. 49.8 B events were collected with plastic, and 53.3 B events with LYSO, respectively. The simulation was distributed in 100 instances and performed in AMD EPYC 9754 128-Core Processor CPUs. In the case of LYSO, the intrinsic radioactivity was not considered as it is also not present in the J-PET's scintillator material. Using the NEMA Image Quality (IQ) phantom (National Electrical Manufacturers Association, 2018) simulations, we investigated the SF for each detector material depending on the lower energy threshold for the photon detection (see Figure 4). The J-PET detector records photons within an energy window of 200-650 keV resulting in a SF of about 43.2% (Kowalski *et al.*, 2016). Simulation studies with the J-PET scanner showed that when the energy threshold is set above 184 keV, detector-scattered coincidences are eliminated (Kowalski *et al.*, 2016). We set the lower energy threshold for LYSO to 408 keV to obtain a SF as close to that of plastic as possible. Thus, an energy window between 408 and 650 keV was applied for LYSO. In both cases the energy resolution was set to 16% (Moskal *et al.*, 2024).

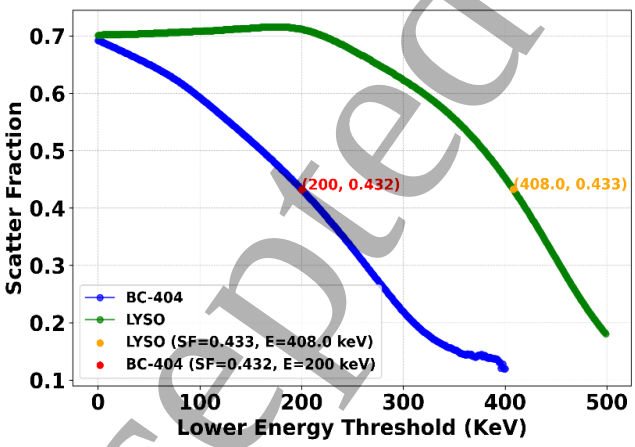

Figure 4: Simulated scatter fraction (SF) using BC-404 (blue) and LYSO (green). The NEMA IQ phantom was simulated. The marks on each graph indicate the lower energy thresholds that result in equal scatter fraction.

The simulated list-mode data of true and scattered events was binned into sinograms, which were scaled to match the measured sinogram of prompt minus random events on a plane-by-plane basis. This step was followed by Gaussian smoothing with a sigma of 4 sinogram bins. The rate of scattered events was computed for each event in the measured list-mode dataset as follows:

$$s_{i,t} = \frac{s_{b,t}^{Sim,Gauss} \cdot f_k}{N_{LOR} \cdot T_{meas}}$$

Here, $s_{i,t}$ is the number of sinogram entries in bin *b* of TOF bin *t*. f_k denotes the scaling factor for plane *k*, T_{meas} is the total measurement duration, and N_{LOR} is the number of possible LORs connecting two detector blocks. The resulting value represents the estimated scatter event rate (in counts per second) attributable to each measured coincidence event. This rate was assigned by matching the LOR index and TOF bin of the measured event to the corresponding entry in the scaled and smoothed scatter sinogram.

The per-event scatter rates were then included in the CASToR list-mode input data file (.Cdf format) as an additional column, alongside the existing event information. Finally, image reconstruction was repeated with the estimated scatter term included in the CASToR input data file.

Imaging Studies

A NEMA IQ phantom was used for image quality assessment which contains six spheres of 10 mm, 13 mm, 17 mm, 22 mm, 28 mm, and 37 mm in diameter filled with a high activity concentration of 42.2 KBq/ml. The activity concentration in the background volume of the phantom was 4.28 KBq/ml resulting in an activity concentration ratio (ACR) between hot spheres and background of approximately $9.85 : 1$. The phantom was scanned for 39 minutes. The activity concentrations and the ACR were estimated using the protocols provided by the experimenters, who filled the phantom. Based on the precision of the measurements of the phantom volume and the radioactive dose, we assume an uncertainty on the ACR of no more than 5%. For the correction of attenuation and scatter and for anatomical reference, a prior CT scan on a separate standalone system was acquired with a commercial GE Discovery MI Gen 2 PET/CT at Jagiellonian Medical University in Krakow and co-registered to the PET FOV.

Then, a human subject evaluation was conducted in a single healthy volunteer: a 62-year-old female subject was scanned upon informed consent on the J-PET scanner for 16 min at 98 minutes post-injection of 155.95 MBq ^{68}Ga-DOTATATE. The range of the scan was from the upper chest to the lower pelvis region. CT-based attenuation and scatter correction were performed in the same way as for the phantom. The J-PET scan was performed after the subject had been scanned on the GE Discovery MI Gen 2 PET/CT for 25 min at 62 min post injection using 8 bed positions with an isocenter different from that of the J-PET scanner. Therefore, the PET and CT images obtained from the GE scanner were aligned to the J-PET isocenter and resampled into the same image grid with 2.5-mm isotropic voxels.

Phantom Evaluation

Key image quality metrics included contrast recovery coefficient (CRC), background variability (BGVar), and residual error in the lung insert, which were assessed for both uncorrected and scatter corrected images. The drawing and placement of the ROIs as well as the analysis followed the standards prescribed by NEMA NU 2-2018 (National Electrical Manufacturers Association, 2018). The CRC values were interpreted with consideration of a 5% systematic uncertainty arising from potential inaccuracies in the phantom filling protocol and, thus, the activity concentration ratios. Additionally, line profiles were extracted through the hot spheres and assessed visually. To visualize the scatter component removed by the correction process, the

difference between the line profiles of the uncorrected and corrected images was computed and a scatter profile was obtained. Finally, we also quantified the contrast to noise ratio (CNR). We placed an ROI in the largest sphere, with a diameter of 33 mm, thereby sparing the boundaries of the sphere to limit the impact of partial volume effects due to image voxelization. We calculated the difference in the activity concentration ratio between the ROI and the background ROIs that were drawn for the above NEMA IQ analysis and divided the result by the standard deviation of the background.

To validate the impact of detector material, all image quality metrics were calculated for both crystal (LYSO) and plastic scintillators. As will be shown in the results and discussion sections, no significant quantitative differences were observed between the two materials. However, LYSO yielded faster performance, and therefore all subsequent MC-based SC procedures – including that of human subject data – were conducted using LYSO exclusively.

Human subject evaluation

A semi-quantitative assessment included noise level estimation via the coefficient of variation measured in the liver, spleen, and lungs, both with and without scatter correction. In addition, qualitative evaluation of scatter removal was performed by analyzing a line profile drawn through the torso region encompassing the liver and spleen. Organ visibility and delineation were assessed visually to provide a qualitative proof-of-principle demonstration of image quality improvements. For both phantom and human subject studies, we calculate the scatter fraction using the scaled sinograms of true and scattered coincidences.

A qualitative comparison between the images generated with the J-PET scanner and the commercial GE Discovery MI Gen 2 PET/CT was performed, the latter of which single scatter simulation (SSS) as SC method (Watson, 2000). We first performed a visual comparison of characteristic image slices through major organs and through the comparison of line profiles. As means of quantitative image quality comparison the average activity concentrations in major organs were calculated using spherical ROIs in the spleen (diameter: 35 mm), the kidney (diameter: 20 mm), and the liver (diameter: 40 mm). Then the ACR between spleen and liver, as well as kidney and liver were calculated for J-PET and GE scanner.

Results

NEMA IQ phantom images

Figure 5 shows the NEMA IQ phantom scan reconstructed with and without scatter correction applied using LYSO as detector material (the comparison to using plastic scintillators in the simulations is shown in the next paragraph). The arrows point to the plastic parts that are only visible due to scatter in the uncorrected image. The right part of Figure 5 shows line profiles in transverse view through the section of the phantom where the spheres are located. The profiles were normalized to the highest value in the non-scatter corrected profile. To visualize the scatter component removed by the correction process, the difference between the line profiles of the uncorrected and corrected images was computed. The resulting scatter component line profile is shown in green color. The height of the peak caused by the large sphere is almost identical in non-corrected and corrected image, while the values inside the lung insert differ considerably: While the non-scatter-corrected image exhibits a minimum line profile value of 0.073, the scatter

corrected image shows a minimum of 0.031, which denotes a reduction of residual activity by 57.5%.

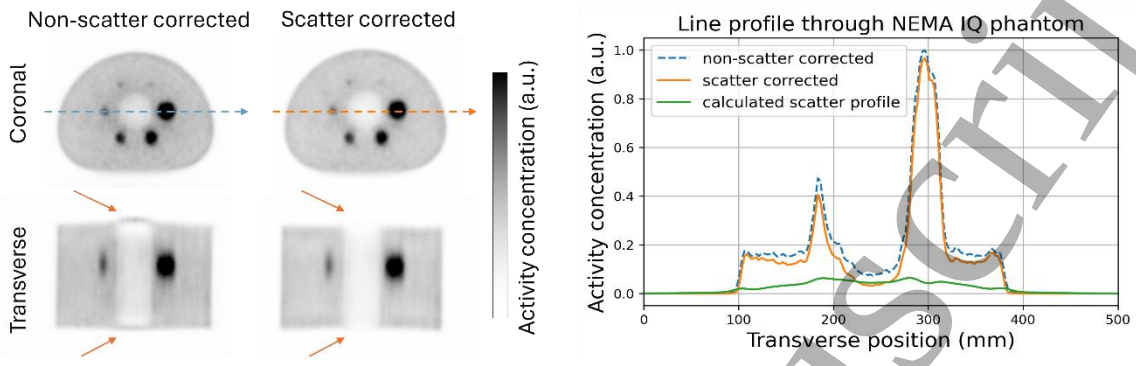

Figure 5: NEMA IQ phantom without and with scatter correction (left). Arrows indicate scatter removal from plastic parts. Line profiles through the phantom's lung insert and two spheres (right). These reconstructions used LYSO as detector material for MC-based SC.

Quantitative Assessment of Phantom Data

THIS FIGURE WAS UPDATED Figure 6 shows CRC (in black) and BGVar (in blue) for both un-corrected (dashed) and corrected images (solid), respectively. The error bars on the CRC curve indicate the systematic uncertainties arising from the uncertainty on the ACR of ±5%. The error bars for BGVar represent statistical uncertainties and were computed using Gaussian error propagation. These results were obtained using LYSO as scintillator material in the MC-based SC algorithm. While no difference within the given uncertainties was observed for the smallest sphere, the scatter corrected images show increasingly higher CRC for larger spheres compared to the non-scatter corrected images. For the 37-mm sphere the scatter-corrected image exhibited a CRC of 62.2%, while the un-corrected image showed a value of only 51.5%, which constitutes a relative improvement of 20.8% when scatter correction is applied. Except for the largest sphere, the BGVar was improved – i.e., lower – throughout all sphere sizes on corrected images compared to their uncorrected counterparts. For instance, the smallest sphere exhibited a reduction of the BGVar from 8.2% to 7.5%, which is a relative improvement of 8.5%. While the largest sphere exhibited an increase in BGVar with a relative difference of +11.1% compared to the uncorrected image, the differences were not statisticically significant within the given statistical uncertainties. These results indicate that no significant amount of noise was introduced into the images through the proposed SC algorithm, and the background varied less and, thus, appeared more uniform.

Finally, the CNR was quantified. On scatter corrected images, a CNR of 7.57 was obtained, while on uncorrected ones the CNR was 6.98. Thus, the scatter corrected image exhibited a larger CNR, with a relative improvement of 8.45% compared to the uncorrected image. The residual error in the lung insert was 49.0% in the uncorrected reconstruction, while 14.1% were obtained when SC was applied. This constitutes a reduction of residual activity by 71.2%.

Validity of Material Choice

At first, the computation times as well as the obtained scatter fraction was investigated, the results of which are listed in Table 1. While simulating the NEMA IQ phantom using LYSO took 9 h and 40 min on our computational infrastructure, the same number of collected coincidences using plastic could only be obtained with 40 times more simulated events which took almost 8 times longer.

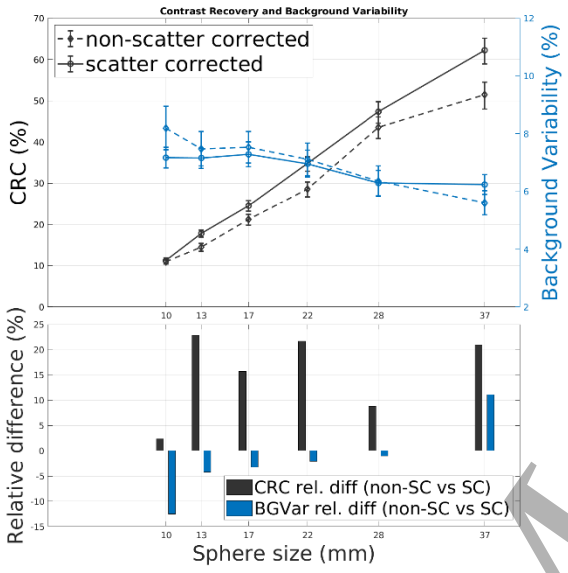

THIS FIGURE WAS UPDATED Figure 6: Top: Contrast recovery coefficient (black) and background variability (blue) of non-scatter corrected, and scatter corrected NEMA IQ phantom scans, respectively. The error bars on CRC curves indicate the systematic uncertainty on the activity concentration in the phantom. The error bars on BGVar represent statistical uncertainties. Bottom: The relative differences in the measured quantities between non-corrected and corrected images.

Table 1: Overview of the simulation times and scatter fractions for phantom and human subject data using LYSO and plastic as detector material.

Subject	*Number of simulated decays*	*Scintillator Material*	*Simulation time*	*Scatter fraction*
Human Subject	5 Billion	LYSO	7 hr, 10 min	50.01%
NEMA-IQ	5 Billion	LYSO	9 hr 40 min	43.27%
NEMA-IQ	200 Billion	BC-404 (Plastic)	69 hr, 22 min	43.24 %

The main goal of this analysis is to investigate the impact of the material choice on quantitative image quality metrics, and thereby to justify the choice of LYSO as scintillator material in all

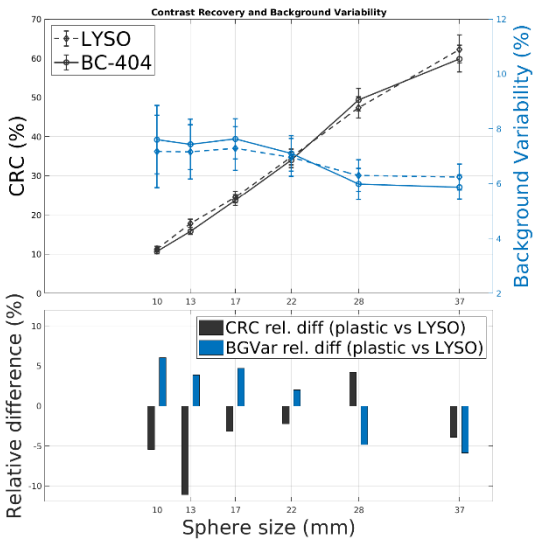

THIS FIGURE WAS UPDATED Figure 7: Top: Contrast recovery coefficient (black) and background variability (blue) of scatter corrected NEMA IQ phantom scans, using LYSO (dashed line) and BC-404 (solid line). The error bars on CRC curves indicate the systematic uncertainty on the activity concentration in the phantom. The error bars on BGVar represent statistical uncertainties. Bottom: The relative differences in the measured quantities between LYSO and BC-404.

MC simulations moving forward. The top part of THIS FIGURE WAS UPDATED Figure 7 shows the CRC (black line) and BGVar (blue line) using LYSO (dashed line) and plastic (solid line) as scintillator material in the simulations. The bottom part of the figure shows the relative differences. The maximum difference in CRC was found for the 13-mm sphere and reached -11.1%, while the smallest difference was found for the 22-mm sphere and was only 2.2%. The relative difference was on average 5.0%. The maximum difference in BGVar was 6.0% for the smallest sphere and 2.0% for the 22-mm sphere. The average was found to be 4.6%.

Then, the CNR was quantified using a 33-mm ROI in the largest sphere. Using LYSO, a CNR of 7.57 was obtained and using plastic material the CNR was 7.35. While the simulation using plastic exhibited a slightly smaller CNR, the relative difference between was only -2.91%. The residual error in the lung insert was 14.1% in case of LYSO and 15.1% when plastic was used. The relative difference therefore was 6.6%.

Scatter Correction Assessment in Human Subject Data

Figure 8 shows the PET/CT fusion image of the human subject reconstructed with and without SC. The arrows point towards major organs such as the liver, spleen and kidneys, which are more clearly delineated in the corrected image. A line profile through the torso shows that scatter between the liver and spleen was successfully reduced with a minimum value of 0.189 in the non-scatter-corrected image and 0.129 in the corrected image. This constitutes a reduction of 31.7%. The steeper fall-off outside the subject in scatter corrected images indicates successful removal of residual scattered activity from non-active regions.

Qualitative and quantitative scanner comparison

Figure 9 shows the coronal and transverse view of the patient scan performed on the commercial GE Discovery MI Gen 2 and the J-PET scanner. The effective axial range of the J-PET is 46 cm, since the first and last 2 cm were cut off due to high noise. The axial range of the GE scan coveres 5 bed positions and is visibly longer. While major organs are visible on both images, the kidneys are better delineated on the GE image, and there is more noise between spleen and liver on the J-PET image. Two line profiles have been drawn through the image as can be seen on the right side of Figure 9. Both profiles were normalized to their maximum value. The first profile is drawn between the liver and the spleen showing a slightly higher activity concentration in the liver in the J-PET image compared to the GE-image. The second profile ranges from the inferior tip of the liver to the left kidney. While the J-PET scanner shows higher noise level and more residual activity in the soft tissue between major organs, the general shape can be very well resolved: in both line profiles the dip in the activity between right kidney and the inferior tip of the liver can be seen at a transverse position of 150 mm – 170 mm.

Finally, the ACR between the spleen and the liver was $(2.45 \pm 0.34)\%$ for the GE scanner and $(2.00 \pm 0.37)\%$ for the J-PET scanner, respectively. The ACR between the right kidney and the liver was $(1.34 \pm 0.11)\%$ and $(1.30 \pm 0.17)\%$, respectively. The uncertainties were calculated using Gaussian error propagation under consideration of the standard deviations on the calculated ROI mean values.

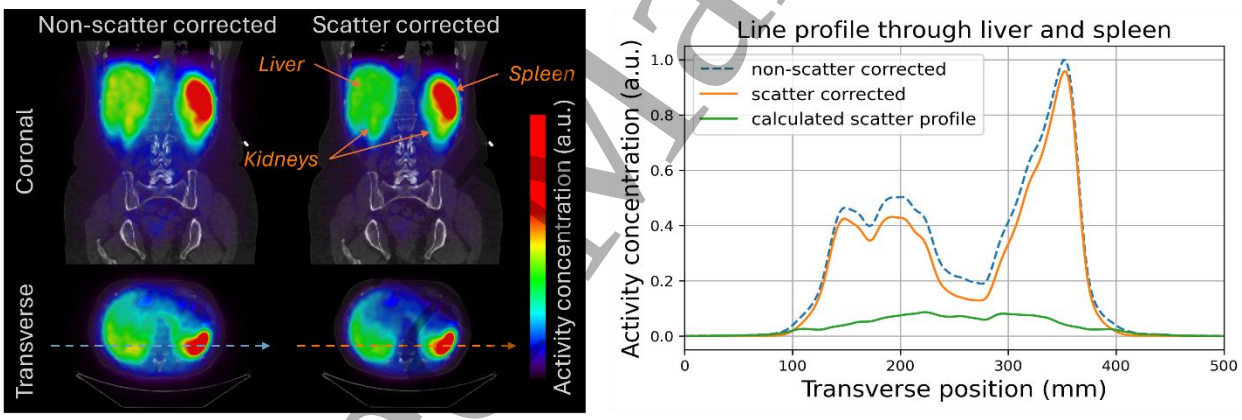

Figure 8: Human subject image without and with scatter correction with indicators for major organs (left). Line profile through the liver and spleen (right).

Discussion

This study demonstrates the feasibility and performance of a Monte Carlo–based scatter correction (SC) method tailored to the modular plastic-scintillator J-PET scanner. Phantom experiments confirmed that the proposed algorithm improves quantitative image quality, with notable increases in contrast recovery coefficients (CRC) and reduced background variability (BGVar), while avoiding additional noise introduction. Human subject images exhibit improved organ delineation in scatter corrected images, while activity concentration ratios between major organs were comparable to a commercial PET/CT scanner. This work is a vital step in bringing PET imaging with plastic-based scanners closer to clinical applications and contributes to the active research field investigating alternative scanner geometries and materials (Godinez *et al.*, 2025). In the following we discuss limitations and potential next steps.

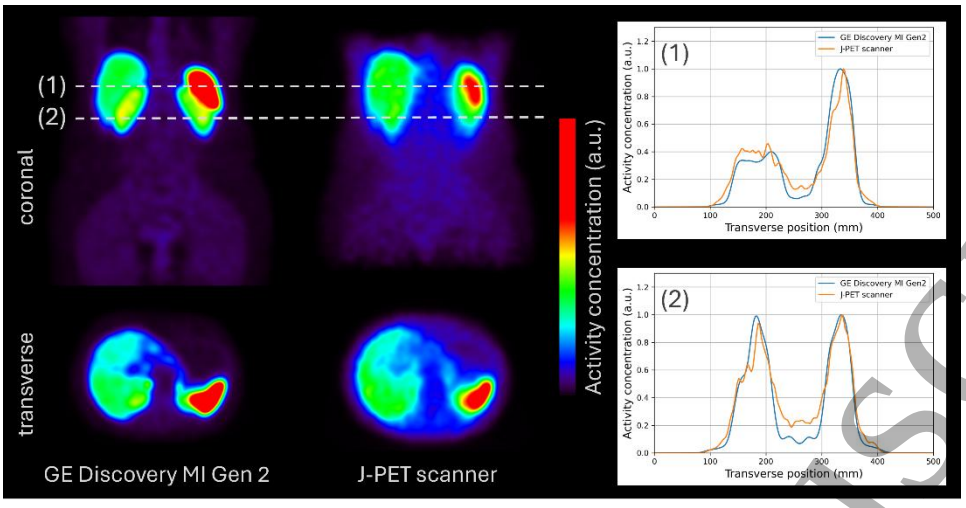

Figure 9: Comparison of scatter-corrected images obtained with a commercial PET scanner and J-PET. The dashed lines indicate the position of the line profiles through liver and spleen (1) and through both kidneys and the inferior tip of the liver (2).

Phantom evaluations

In phantom measurements, the spatial resolution in the transverse plane appeared comparable to that of conventional short axial FOV PET scanners. However, due to the limited intrinsic spatial resolution of the plastic scintillator strips, axial resolution was noticeably reduced (Ardebili and Moskal, 2024). This limitation manifested as visible shape distortion in the spheres. Nonetheless, the scanner demonstrated good scatter clearance within the plastic components of the phantom. A slight overcorrection was observed at the top and bottom edges of the phantom, potentially caused by multiple factors. One plausible explanation is imperfect normalization, which appears more challenging with scintillator strips compared to crystals, and achieving uniform sensitivity across the scanner axis might be more complex.

At low count rates, scatter correction becomes increasingly difficult due to elevated statistical noise, often leading to residual activity in cold regions (Zaidi, H. and Koral, K.F., 2006). Nevertheless, in this study, a pronounced reduction in residual activity was observed in the lung insert, despite the low count conditions.

The estimation of the ACR between hot spheres and warm phantom background was determined retrospectively according to the fill protocol, with an assumed uncertainty of approximately 5%. This uncertainty was incorporated as a systematic component in the error estimation of the CRC. Nevertheless, the increase in CRC for the 37-mm and 28-mm spheres in scatter corrected images compared to uncorrected ones remains significant within the given uncertainties, as evidenced by the error bars shown in THIS FIGURE WAS UPDATED Figure 6.

The measured scatter fraction (SF) was 43.3% in the NEMA IQ phantom and 50.0% in the human subject scan. The phantom result is comparable to prior phantom simulations who reported a SF of $41.7 \pm 0.2\%$ (Ardebili, 2023) for similar configurations. Our results are also in good agreement with the work by Kowalski et al. (Kowalski *et al.*, 2016) who investigated the SF in J-PET depending on the lower energy threshold using GATE simulations. For a lower threshold of 200 keV their work predicts a SF of approximately 45%.

We further evaluated the use of LYSO crystals in the simulations as a surrogate for the native J-PET detector material BC-404 (plastic), with the aim of reducing computational demands. As can be seen in the CRC and BGVar this substitution introduced only minor deviations in SC accuracy, while considerably improving simulation efficiency by nearly one order of magnitude (see table 1). Simulating with LYSO instead of BC-404 reduces the computation time by a factor of 8. Although both CRC and BGVar exhibited individual outliers, the mean deviation between LYSO and plastic was limited to 5% (CRC) and 6% (BGVar). For further acceleration of simulation run times, one could use the artificial material "absorbium" provided by SimSET, which provides 100% attenuation for impinging 511-keV photons through forced interaction. This step requires additional validation and is work in progress.

Additional factors may explain the minor deviations in CRC (THIS FIGURE WAS UPDATED Figure 7): numerical assessments have demonstrated that CRC is sensitive to the precision of ROI placement during image analysis. A misalignment as small as half a voxel can alter CRC values by up to 10%, depending on voxel size (Bayerlein *et al.*, 2023). Moreover, statistical image noise can introduce fluctuations of several percent, even when comparing images reconstructed under identical noise conditions.

Human subject evaluations

Comparison of scatter-corrected and uncorrected images of the human subject revealed reduced residual activity between major organs in the corrected images, accompanied by improved organ delineation. Line profile analysis further demonstrated a marked reduction of residual activity in cold regions, such as areas outside the body contour. While the qualitative improvements in scatter suppression between major organs are evident in the human dataset, the lack of ground truth and absolute activity concentration values prevent a more quantitative evaluation of human subject images at this point.

Quantitative comparison with a commercial short axial FOV scanner demonstrated comparable activity concentration ratios across major organs. However, the lower count density of the J-PET system resulted in increased image noise, which in turn made SC substantially more challenging, as evidenced by the higher residual activity observed between the spleen and liver compared to the commercial scanner. Since there was only a small 6.6-% difference in the residual error in the lung insert when using LYSO compared to plastic, the material choice is not a major contributor to residual activity in the human subject images. Potential strategies to mitigate these limitations include longer acquisition times, administration of higher tracer activities, or the application of advanced reconstruction techniques such as deep learning-based kernel methods (Li and Wang, 2022).

Limitations

This study has several limitations that should be acknowledged. First, the imaging evaluation was performed in a single human subject, providing only a proof-of-principle demonstration without statistical generalizability. Second, quantitative calibration of the J-PET scanner to activity concentrations or standardized uptake values (SUVs) was not available at the time of this work, which restricted inter-scanner comparisons to relative ratios. Third, although the substitution of LYSO for BC-404 in the simulations substantially reduced computation time, it represents an approximation and does not fully capture the detector physics of plastic scintillators. Fourth, the initial image estimate – corrected for randoms and attenuation but not

for scatter – is used as activity distribution map for the Monte Carlo-simulations in SimSET. This initial image does not account for scatter, and thus, the resulting activity map is inherently biased and may affect the accuracy of the scatter estimate. An iterative approach of re-running the MC-simulation using the first scatter corrected image might improve quantitative accuracy. Such an approach has been successfully tested before on the EXPLORER scanner and is subject of ongoing work. Finally, phantom acquisitions employed a sphere-to-background activity ratio different from the NEMA standard, limiting direct comparability with prior reports (e.g., (Moskal *et al.*, 2021)). Future studies will address these aspects by incorporating SUV calibration, standardized NEMA acquisition protocols, multi-subject datasets, and additional validation of the surrogate simulation approach. These steps will be essential to establish a foundation for subsequent methodological and clinical validation.

Conclusion

Despite the above limitations, this work demonstrates that Monte Carlo–based scatter correction can substantially improve image quality and quantitative accuracy in the J-PET scanner. Phantom experiments confirmed significant improvements in contrast recovery and background uniformity, while human subject imaging showed reduced residual scatter and improved organ delineation. Comparisons with a commercial PET/CT indicated broadly consistent activity ratios across major organs, albeit with increased noise due to the lower count density inherent to low-sensitivity systems.

Overall, the successful implementation of scatter correction represents a critical milestone for J-PET, bringing this novel long-axial FOV, plastic scintillator-based scanner closer to enabling clinically relevant quantitative PET imaging. The next generation of the J-PET scanner which is under construction (Moskal *et al.*, 2021), is expected to overcome the limitation of lower sensitivity and spatial resolution by the application of two scintillator layers and an additional layer of wavelength shifters (Smyrski *et al.*, 2014, 2017).

Acknowledgements

We acknowledge support from the National Science Centre of Poland through grants MAESTRO no. 2021/42/A/ST2/00423 (P.M.), OPUS no. 2021/43/B/ST2/02150 (P.M.), OPUS24+LAP no. 2022/47/I/NZ7/03112 (E.S.), SONATA no. 2023/50/E/ST2/00574 (S.S.), the Ministry of Science and Higher Education through grant no. IAL/SP/596235/2023 (P.M.), European Union within the Horizon Europe Framework Programme (ERC Advanced Grant POSITRONIUM no. 101199807), the SciMat and qLife Priority Research Areas budget under the program Excellence Initiative – Research University at Jagiellonian University (P.M. and E.S.), the Research Support Module as part of the Excellence Initiative – Research University program at Jagiellonian University (M.D.). We also acknowledge Polish high-performance computing infrastructure PLGrid (HPC Center: ACK Cyfronet AGH) for providing computer facilities and support within computational grant no. PLG/2024/017688.

Ethical Statement

The participant's data was acquired after informed written consent. The studies (approved by bioethics committees, agreement: 1072.6120.92.2023 (NCT06242119)) were conducted at the University Hospital in Krakow.

Disclosures

P. Moskal is a holder of patents relevant to this work, in particular on PET from plastic scintillators.

References

Ardebili, F., Tayefi and Moskal, P. (2024) "Assessing the Spatial Resolution of the Modular J-PET Scanner using the Maximum-Likelihood Expectation-Maximization (MLEM) algorithm," *Bio-Algorithms and Med-Systems*, 20(Special Issue). Available at: https://bamsjournal.com/article/548095/en (Accessed: November 1, 2025).

Ardebili, F.T. (2023) *Evaluation of the NEMA Characteristics for the Modular J-PET Scanner*. Jagiellonian University. Available at: https://koza.if.uj.edu.pl/files/7a5bfa96073653144178d0504fb23780/FTA_thesis.pdf (Accessed: October 4, 2025).

Ardebili, F.T., Niedźwiecki, S. and Moskal, P. (2023) "Evaluation of Modular J-PET sensitivity," *Bio-Algorithms and Med-Systems*, 19(1), pp. 132–138. Available at: https://doi.org/10.5604/01.3001.0054.1973.

Badawi, R.D. and Marsden, P.K. (1999) "Developments in component-based normalization for 3D PET," *Physics in Medicine & Biology*, 44(2), p. 571. Available at: https://doi.org/10.1088/0031-9155/44/2/020.

Bayerlein, R. *et al.* (2023) "Numerical investigation reveals challenges in measuring the contrast recovery coefficients in PET," *Physics in Medicine & Biology*, 68(21), p. 215013. Available at: https://doi.org/10.1088/1361-6560/ad00fa.

Bayerlein, R. *et al.* (2024) "Development of a Monte Carlo-based scatter correction method for total-body PET using the uEXPLORER PET/CT scanner," *Physics in Medicine & Biology*, 69(4), p. 045033. Available at: https://doi.org/10.1088/1361-6560/ad2230.

Carney, J.P.J. *et al.* (2006) "Method for transforming CT images for attenuation correction in PET/CT imaging," *Medical Physics*, 33(4), pp. 976–983. Available at: https://doi.org/10.1118/1.2174132.

Das, M., Bayerlein, R., and et al. (2024) "Development of correction techniques for the J-PET scanner," *Bio-Algorithms and Med-Systems*, 20(1), pp. 101–110. Available at: https://doi.org/10.5604/01.3001.0054.9362.

Godinez, F. *et al.* (2025) "Total Body PET/CT: Future Aspects," *Seminars in Nuclear Medicine*, 55(1), pp. 107–115. Available at: https://doi.org/10.1053/j.semnuclmed.2024.10.011.

Gurunath Bharathi, P. *et al.* (2025) "Transformative Advances in PET Imaging: From FDG to Total Body Scanners, Novel Tracers and AI-Driven Precision Medicine," *Bio-Algorithms and Med-Systems*, 21(1), pp. 40–57.

Kapłon, Ł. *et al.* (2025) "Quality control of plastic scintillators for the total-body J-PET scanner," *Journal of Instrumentation*, 20(09), p. P09019. Available at: https://doi.org/10.1088/1748-0221/20/09/P09019.

Kowalski, P. *et al.* (2016) "Scatter fraction of the J-PET tomography scanner," *Acta Physica Polonica B*, 47(2), p. 549. Available at: https://doi.org/10.5506/APhysPolB.47.549.

Li, S. and Wang, G. (2022) "Deep Kernel Representation for Image Reconstruction in PET," *IEEE Transactions on Medical Imaging*, 41(11), pp. 3029–3038. Available at: https://doi.org/10.1109/TMI.2022.3176002.

Merlin, T. *et al.* (2018) "CASToR: a generic data organization and processing code framework for multi-modal and multi-dimensional tomographic reconstruction," *Physics in Medicine & Biology*, 63(18), p. 185005. Available at: https://doi.org/10.1088/1361-6560/aadac1.

Moskal, P. *et al.* (2016) "Time resolution of the plastic scintillator strips with matrix photomultiplier readout for J-PET tomograph," *Physics in Medicine & Biology*, 61(5), p. 2025. Available at: https://doi.org/10.1088/0031-9155/61/5/2025.

Moskal, P. *et al.* (2021) "Simulating NEMA characteristics of the modular total-body J-PET scanner—an economic total-body PET from plastic scintillators," *Physics in Medicine & Biology*, 66(17), p. 175015. Available at: https://doi.org/10.1088/1361-6560/ac16bd.

Moskal, P. *et al.* (2024) "Positronium image of the human brain in vivo," *Science Advances*, 10(37), p. eadp2840. Available at: https://doi.org/10.1126/sciadv.adp2840.

National Electrical Manufacturers Association (2018) "NEMA standards publication NU 2-2018 – performance measurements of positron emission tomographs (PET)." Rosslyn, VA.

Pépin, A. *et al.* (2011) "Normalization of Monte Carlo PET data using GATE," in *2011 IEEE Nuclear Science Symposium Conference Record*. *2011 IEEE Nuclear Science Symposium Conference Record*, pp. 4196–4200. Available at: https://doi.org/10.1109/NSSMIC.2011.6153804.

Sharma, S. *et al.* (2023) "Efficiency determination of J-PET: first plastic scintillators-based PET scanner," *EJNMMI Physics*, 10(1), p. 28. Available at: https://doi.org/10.1186/s40658-023-00546-7.

Smyrski, J. *et al.* (2014) "Application of WLS strips for position determination in strip PET tomograph based on plastic scintillators," *Bio-Algorithms and Med-Systems*, 10(2), pp. 59–63. Available at: https://doi.org/10.1515/bams-2013-0103.

Smyrski, J. *et al.* (2017) "Measurement of gamma quantum interaction point in plastic scintillator with WLS strips," *Nuclear Instruments and Methods in Physics Research Section A: Accelerators, Spectrometers, Detectors and Associated Equipment*, 851, pp. 39–42. Available at: https://doi.org/10.1016/j.nima.2017.01.045.

Vandenberghe, S., Moskal, P. and Karp, J.S. (2020) "State of the art in total body PET," *EJNMMI Physics*, 7(1), p. 35. Available at: https://doi.org/10.1186/s40658-020-00290-2.

Watson, C.C. (2000) "New, faster, image-based scatter correction for 3D PET," *IEEE Transactions on Nuclear Science*, 47(4), pp. 1587–1594. Available at: https://doi.org/10.1109/23.873020.

Zaidi, H. (2000) "Comparative evaluation of scatter correction techniques in 3D positron emission tomography," *European Journal of Nuclear Medicine*, 27(12), pp. 1813–1826. Available at: https://doi.org/10.1007/s002590000385.

Zaidi, H. and Koral, K.F. (2006) "Scatter Correction Strategies in Emission Tomography," in *Quantitative Analysis in Nuclear Medicine Imaging*. Springer. Available at: https://doi.org/10.1007/0-387-25444-7_7.

Zaidi, H. and Montandon, M.-L. (2007) "Scatter Compensation Techniques in PET," *PET Clinics*, 2(2), pp. 219–234. Available at: https://doi.org/10.1016/j.cpet.2007.10.003.